

Behavior and properties of helium cavities in ductile-phase-toughened tungsten irradiated with He⁺ ions at an elevated temperature

Weilin Jiang^{a,*}, Libor Kovarik^a, Karen Kruska^a, Yucheng Fu^a, Zhihan Hu^b, Lin Shao^b, Wahyu Setyawan^a

^a *Pacific Northwest National Laboratory, Richland, WA, United States*

^b *Department of Nuclear Engineering, Texas A&M University, College Station, TX, United States*

HIGHLIGHTS

- He cavities in He⁺ ion irradiated 87R DPT W are examined at an atomic-level resolution.
- The average diameter (~4.05 nm) of the cavities in NiFeW is ~2.7 times that in W.
- The number density of the cavities in NiFeW is an order of magnitude lower than in W.
- He atoms are under-pressurized in the cavities in NiFeW.
- He energy-loss shift is proportional to the He density with a slope comparable to that for steel.

ABSTRACT

Ductile-phase toughened tungsten (DPT W) composites have demonstrated a great potential for plasma-facing components in fusion power systems. These materials can retain the outstanding thermomechanical properties of W while significantly enhancing the fracture toughness. The DPT W composite in this study consists of W particles (88 wt.%) embedded in a ductile NiFeW (12 wt.%) solution matrix. Irradiation of the composite was performed with 90 keV He⁺ ions to 1.0×10^{17} He⁺/cm² at 973 K. The He cavities formed in both W and NiFeW phases are examined using convergent-beam scanning transmission electron microscopy (CB-STEM) at an atomic-level resolution. Full-range depth profiles of the He cavity diameters and number densities are analyzed. The results show that the average cavity diameter in NiFeW is ~2.7 times that in W, while the number density is an order of magnitude lower. A quantitative analysis of the He density and pressure in the cavities is also achieved using STEM electron energy loss spectroscopy (STEM-EELS) mapping. The He atoms in the cavities in NiFeW are found to be under-pressurized, while those in similar-sized cavities in W are not detectable. The He energy-loss shift exhibits a linear relationship with the He density in cavities in NiFeW, with the slope comparable to that for martensitic steel.

Keywords: Helium cavity, CB-STEM, STEM-EELS, ion irradiation, ductile-phase-toughened tungsten

* Corresponding author. *E-mail address*: weilin.jiang@pnnl.gov (W. Jiang).

1. Introduction

Tungsten (W) has outstanding thermomechanical properties for plasma-facing components of fusion power systems [1-6]. However, pure W has low fracture toughness at room temperature and its ductile to brittle transition temperature (DBTT) increases with irradiation damage [7,8]. Ductile-phase toughened tungsten (DPT W) composites, often referred to as tungsten heavy alloys (WHAs), can exhibit significantly higher fracture toughness than pure W [9-12], while largely retaining the favored W properties suitable for fusion applications. As an example, 90W-7Ni-3Fe DPT W composite consists of predominant brittle-phase W particles embedded in a small fraction of ductile-phase matrix of Ni-based NiFeW solid solution. The ductile phase can prevent or inhibit crack propagation by facilitating crack bridging, deflection, and branching [9]. The continuous nature of the NiFeW phase provides a ductile tearing path through the material, limiting crack progression through the W phase and at the heterogeneous interface. Microcracking at the interphase boundaries is predominantly blunted and arrested by the ductile phase with little to no interfacial de-bonding [12]. The composites exhibit an extraordinary combination of strength, ductility, and toughness and have a great potential to withstand the extreme fusion reactor environment [13].

Irradiation of DPT W with 14.1 MeV neutrons from the $^3\text{T(d,n)}^4\text{He}$ fusion reaction produces atomic displacements, resulting in generation of lattice defects and creates transmutation products, including He from Ni, Fe and W [14,15]. Diffusion and interaction of He atoms and vacancies could lead to nucleation and growth of He cavities in DPT W. The critical parameters controlling the evolution of the cavity size and number density during He accumulation by elemental transmutation or He^+ ion implantation include temperature, He accumulation rate, displacement rate, He concentration, and dose [16]. In general, the presence of He cavities in metals causes considerable concerns because it can substantially deteriorate the material's mechanical properties. At low temperatures ($T < 0.4T_m$ with T_m being the melting point) He cavities can form in the grain interior, leading to hardening and embrittlement; at higher temperatures ($T > 0.5T_m$) they can aggregate at grain boundaries to increase the embrittlement of the material. This property degradation can occur even at low He concentrations [17,18]. At very high He [19] (or H [20,21]) concentrations in W, blisters can form, and surface exfoliation may occur. Therefore, it is crucial to study the He behavior in candidate fusion materials, such as DPT W [9].

Conventional transmission electron microscopy (TEM) under a defocus condition has been extensively applied to characterize the size of He cavities in various materials based on the Fresnel fringe contrast. A defocus condition is necessary because the bubble edges hardly create any contrast at focus, even if a contrast aperture is used. However, the actual He cavity size is obscured in defocus conditions and the observed cavity size must be corrected. The correction of measured diameters has been demonstrated based on the reported simulation results in our previous study [18]. If the areal number density (a product of volumetric density and local foil thickness) of nano-sized cavities is high, there is a high probability for the cavity images to overlap across the TEM foil thickness (typically ~100 nm) due to projection. Therefore, projection can lead to an error in estimating the cavity number density and size distributions when small cavities are partially or entirely covered up by larger ones and become invisible in the TEM image. This study explores a convergent-beam scanning transmission electron microscopy (CB-STEM) methodology to minimize the projection effects. In contrast to the conventional TEM [18,22], the CB-STEM technique uses a convergent beam that limits the imaging depth of field to only 20-40 nm, regardless of the local thickness. The resulting image will show the actual size of the cavity at an atomic-level resolution with a significantly lower probability of cavity overlapping, thus allowing for a

more accurate analysis of the number density and size distributions of the cavities. In this study, we attempted to apply CB-STEM to quantify the distributions of He cavity diameters and volumes as well as number densities as a function of depth in both W and NiFeW phases within a hot-rolled, 87% thickness-reduced DPT W (87R DPT W) sample in an emulated fusion environment. In this report, “cavity” refers to a He-filled or empty cavity, while “bubble” designates a pressurized He cavity [23].

In addition, we also quantify the He density and pressure in nano-sized cavities. These quantities reflect the extent of the He gas retention in the material and can have a significant effect on the mechanical properties of the material. Walsh, Yuan and Brown [24] have developed a method for measuring the He density and pressure in small bubbles in solid materials based on electron energy loss spectroscopy (EELS). This method has been successfully applied to characterize He bubbles in a tritiated Pd₉₀Pt₁₀ alloy [25] and a He⁺ ion implanted martensitic steel [26]. It has also been extended to study the association of H with He bubbles in zirconium [27] as well as a simultaneous analysis of He and T inside bubbles in beryllium [28]. Molecular dynamics (MD) simulations of He bubbles in Ni have been reported [29]. There are also simulation studies to calculate the He bubble pressure in tungsten [30–35]. Experimental data for He densities in bubbles in pure Ni have been compiled [36]. To our knowledge, however, quantifications of He density or pressure in cavities in either W or NiFeW have not yet been reported to date.

2. Experimental procedures

2.1. SRIM simulation and ion irradiation

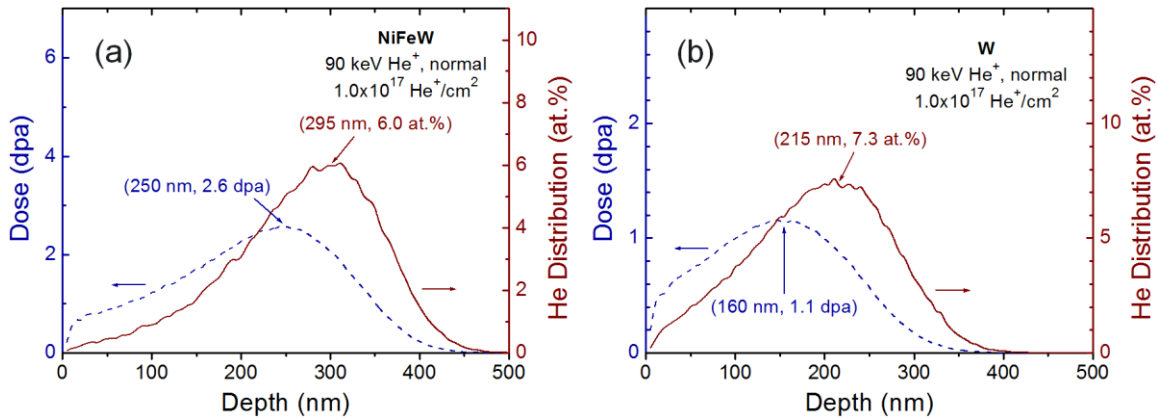


Fig. 1. Depth profiles of the He atomic percentage and dose from quick K-P SRIM13 simulations for irradiation with 90 keV He⁺ ions to 1.0×10^{17} He⁺/cm² in (a) NiFeW and (b) W.

As described previously [18], the material in this study consists of brittle W particles (88 wt.%) embedded in a ductile NiFeW (12 wt.%) solution matrix with 54.68 wt.% (63.83 at.%) Ni, 22.57 wt.% (27.69 at.%) Fe, and 22.75 wt.% (8.48 at.%) W. In order to estimate dose rate and He concentration distributions in W and NiFeW, quick Kinchin-Pease (K-P) SRIM13 (Stopping and Range of Ions in Matter, version 2013 [37]) simulations were carried out for 90 keV He⁺ ions in W and NiFeW, where the threshold displacement energies of $E_d(\text{W}) = 90$ eV and $E_d(\text{Ni}) = E_d(\text{Fe}) = 40$ eV were adopted [38]. The lattice binding energy was set to 0 eV [39]. Note that if $E_d(\text{W})$ were taken as 40 eV for the W sublattice in NiFeW, the total displacement rate would increase by only 5%. In the simulation, theoretical densities of

body-centered cubic W and face-centered cubic NiFeW were assumed to be 19.25 g/cm³ (6.3×10²² at./cm³) and 9.50 g/cm³ (8.3×10²² at./cm³), respectively. The simulation results for 1.0×10¹⁷ He⁺/cm² in W and NiFeW are shown in Fig. 1. The peak dose corresponds to 2.6 dpa at 250 nm in NiFeW and 1.1 dpa at 160 nm in W. The maximum He concentration is 6.0 at.% at 295 nm in NiFeW and 7.3 at.% at 215 nm in W. Note that SRIM simulations are performed at the temperature of 0 K. The real He depth profiles are expected to be broader due to He diffusion during ion irradiation at an elevated temperature. In addition to the interaction between He atoms and vacancies, causing He cavities to nucleate and grow, some of the He atoms also likely diffuse to the surface and release from the sample.

Ion irradiation was performed with 90 keV He⁺ ions at normal incidence to 1.0×10¹⁷ He⁺/cm² at 973 K. The low ion energy for ion irradiation was chosen for the convenience of damage profiling near the surface region. A resistance heater was located behind a copper plate on which the sample was mounted. A thermocouple was clamped on the sample surface for temperature measurement. Irradiation was manually interrupted about every 15 min to check and, if necessary, adjust the beam current, which was found to be reasonably stable. The beam current is arithmetically averaged over the time period. In spite of this procedure, the absolute ion fluence is still subject to an error of up to 10% or greater. The average ion flux over a rastered area of 5 mm × 10 mm was ~2×10¹³ (He⁺/cm²)/s.

2.2. Sample preparation and characterization

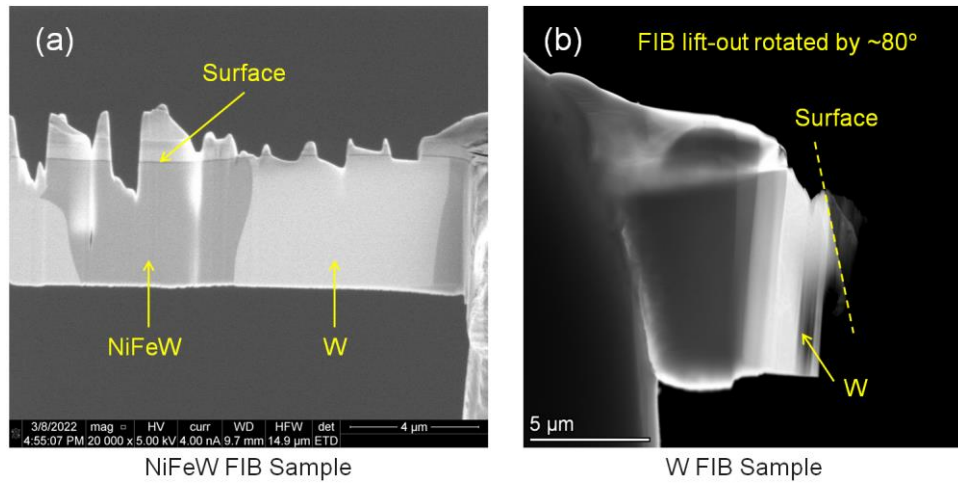


Fig. 2. FIB samples for TEM examinations of (a) NiFeW and (b) W in 87R DPT W irradiated with 90 keV He⁺ ions to 1.0×10¹⁷ He⁺/cm² at 973 K.

Two separate cross-sectional TEM samples were prepared to examine He cavities in the irradiated 87R DPT W using an FEI Quanta 3D FEG dual-beam focused ion beam (FIB) microscope. Fig. 2 shows the scanning electron microscopy (SEM) images for the two FIB samples, each having a distinct contrast of W (bright) and NiFeW (dark) phases. Regions with NiFeW and W interphases were selected to cap with electron- and ion-deposited Pt layers to protect the surface prior to the FIB process. One lamella for cavity examination in NiFeW was extracted using a standard lift-out procedure with a Ga⁺ ion beam and attached to a Cu grid. Windows in the lamella were thinned with the Ga⁺ ion beam at 30 kV and were finished in a final low-energy polishing step with the beam energy reduced to 2 kV. The sample in Fig. 2(a) has thin NiFeW regions (~100 nm) over the entire irradiation region and some extremely thin zones

(20-30 nm) suitable for CB-STEM and STEM-EELS of He cavities, respectively. As an even thinner foil is required for STEM-EELS of the He cavities in W that has a lower sputtering rate than NiFeW, an additional FIB sample for examination of cavities in W was prepared, as shown in Fig. 2(b). Because the W phase is more resistant to the ion-beam sputtering than the protective Pt cap, obtaining the ultra-thin samples necessary for STEM-EELS analysis proved challenging without losing the He irradiated surface layer. Therefore, a modified lift-out process was used by mounting the lift-out on a Cu grid with a rotation by $\sim 80^\circ$ and thinning along a direction nearly parallel to the sample surface. It was found that rather than thinning the new “surface” of the sample, the best results were obtained when the lowest portion of the rotated FIB lamella was thinned, producing a zone with ~ 10 nm thick W foil suitable for STEM-EELS.

The FIB samples were examined using a probe aberration-corrected 300 kV Thermo Fisher Scientific Themis STEM microscope with a spatial resolution of 0.05 nm, equipped with a high-performance EELS detection system. High-angle annular dark-field (HAADF) CB-STEM with a convergence semi-angle of 25 mrad and a collection semi-angle of 52 mrad was performed at an accelerating voltage of 300 kV and a scanning increment step between 0.032 and 0.140 nm. STEM-EELS mapping was performed also at 300 kV with a collection semi-angle of 38.5 mrad and a scanning step between 0.073 and 0.23 nm. Compared to lower voltage (e.g., 200 kV) imaging, utilization of 300 kV STEM-EELS for He cavities provides several advantages, including (1) a decreased loss of He atoms in a cavity due to ballistic collisions [23] during EELS measurement, (2) likely occurrence of He K-shell ionization for the He atoms in the cavities of this study, and (3) less stringent requirement for minimal foil thicknesses. The STEM and EELS data were analyzed using the Gatan Microscopy Suite 3.

3. Analytical methods

3.1. Cavity diameter, volume and number density

The He cavity profiles as a function of depth are analyzed using an in-house developed image processing algorithm. Various atomic-level resolution HAADF CB-STEM images were taken and stitched over the entire irradiation depth region. The CB-STEM images were processed through several steps. The atomic lattice contrast in the image of the host material is first removed via an FFT process. Then, a background correction is performed to remove contrast differences resulting from uneven illumination. Finally, the grainy Poisson noise is removed, leading to a high-contrast cavity image. A projection of the cavity size, shape, and depth within the sample can be extracted from the processed images. For an i th single cavity, the area A_i is determined by counting the occupied pixels in the image. Assuming each of the individual cavities is a sphere, the cavity diameter $d_i = \sqrt{4A_i/\pi}$ and volume $V_i = \pi d_i^3/6$ can be calculated. Overlapping cavities from different depths in the foil are separated into two or more cavities by reconstructing the partially visible cavities via boundary segments to distinguish each individual cavity for an accurate area calculation. Details of the segmentation and reconstruction methods will be reported separately. Using this method, the cavity diameter, volume and number density as a function of depth have been determined in both the NiFeW and W phases of the irradiated 87R DPT W. The average cavity diameter is defined as $D_0 = \Sigma_i d_i/n$, where n is the total number of the cavities within a specific image area, and the average volume $V_0 = \Sigma_i V_i/n$. The depth for D_0 and V_0 is assigned as the geometrical center of the image.

3.2. He density and pressure in a cavity

This study uses the Walsh-Yuan-Brown [24] and Brutzel-Chartier [40] methods to quantify the He density and pressure in the cavities in 87R DPT W. An EELS method for measurement of the He density in a nanometer-sized cavity was proposed based on the scattering probability of an electron [24]:

$$I_{\text{He}}/I_{\text{Z}} = \exp(d/\lambda) - 1 \approx d/\lambda = \sigma n d, \text{ or}$$

$$n \approx I_{\text{He}}/(I_{\text{Z}}\sigma d), \text{ when } d \ll \lambda, \quad (1)$$

where n is the density of the He atoms in the cavity, σ is the partial inelastic cross-section for He excitation, d is the bubble thickness in the direction of the electron beam, I_{He} and I_{Z} are the integrated intensities of the He core-loss and zero-loss peaks, respectively, and $\lambda (= 1/(\sigma n))$ is the mean free path for scattering in He gas. The pressure inside the bubble can be determined by the equation of state (EOS) under a rigid sphere model [41]:

$$P = k_{\text{B}}nT (1 + y + y^2 - y^3)/(1 - y)^3, \quad y = \pi n D^3/6, \quad (2)$$

where k_{B} is the Boltzmann's constant, T is the absolute temperature, y is the volumetric fraction of gas, and D is the rigid-sphere diameter in Brearley-MacInnes model [42]. More recently, the D value is determined [40] based on the Tang-Toennies potential:

$$D = 2.973[0.817 - 0.038\ln(T/10.985)], \quad (3)$$

where the units of D and T are in Å and K, respectively. EELS measures the He density through the scattering probability of an electron that loses its kinetic energy by exciting or ionizing a 1s electron in He. The $1s \rightarrow 2p$ transition of a free He atom is located at 21.218 eV while 1s electron ionization is at 24.59 eV. The EELS spectrum in the low energy region (<50 eV) consists of a zero-loss peak, a plasmon peak from the host material and a He core-loss edge that is overlapped with the plasmon peak. In order to obtain the He edge, two EELS spectra are taken, one of which from the bubble center and the other from the matrix close to the bubble. After suitable yield normalization and subtraction of the latter from the former, the difference is the He core-loss peak.

4. Results and discussion

4.1. Formation and distribution of He cavities

Stitched depth-dependent HAADF CB-STEM images of He cavities in NiFeW within an irradiated DPT W are shown in Fig. 3(a). The cavity contrast is stronger closer to the top surface of the foil, which emerges as a result of the foil thickness difference. In general, He cavities show a darker contrast

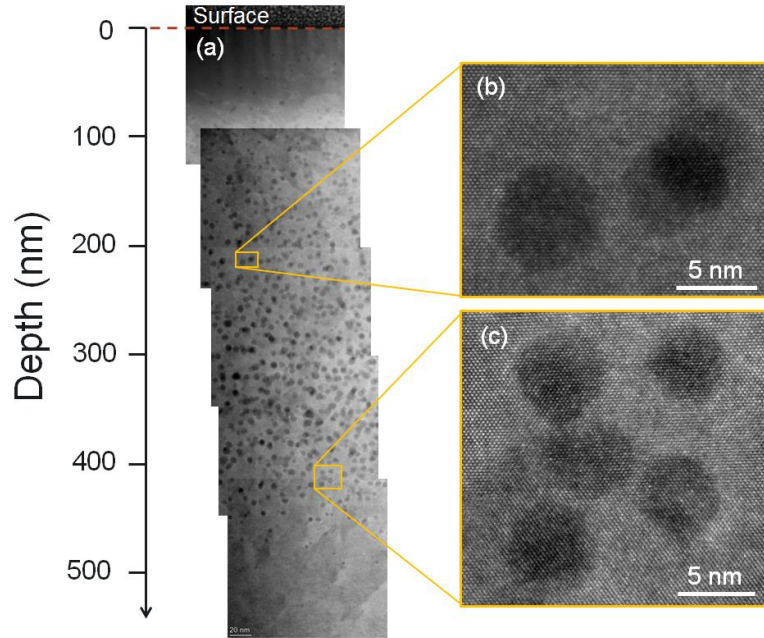


Fig. 3. (a) Atomic-level resolution depth profile of the He cavities in NiFeW within 87R DPT W irradiated to 1.0×10^{17} He⁺/cm² at 973 K and zoomed-in view of the cavities near (b) damage peak and (c) ion projected range.

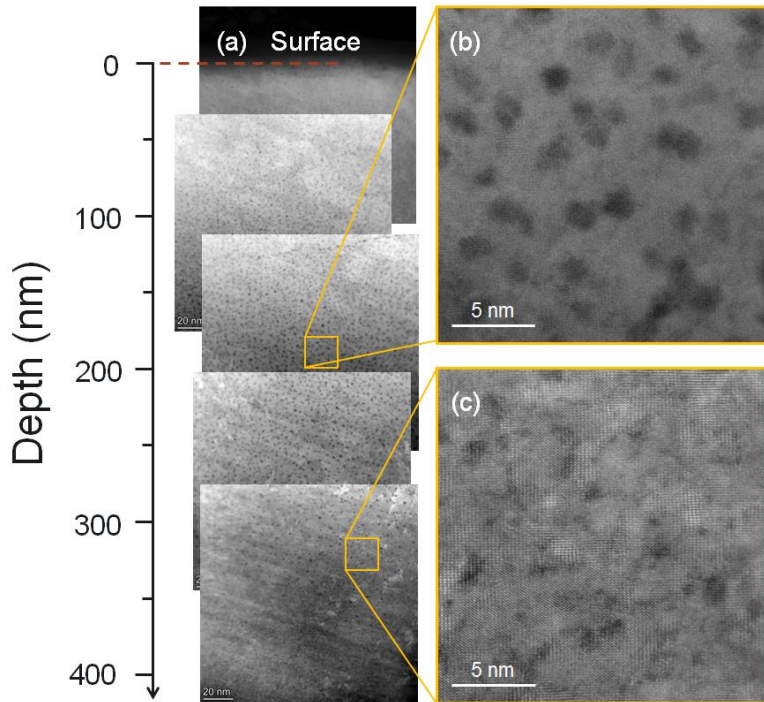


Fig. 4. (a) Atomic-level resolution depth profile of the He cavities in W within 87R DPT W irradiated to 1.0×10^{17} He⁺/cm² at 973 K and zoomed-in view of the cavities near (b) damage peak and (c) ion projected range.

compared to the surrounding metal in the HAADF imaging mode due to smaller thickness in the cavity region. Over the depth of focus (20-30 nm) starting from the foil surface, cavities are observed in actual size at an atomic-level resolution. This is evidenced by the images near the depths of the damage peak

and ion projected range [Figs. 3(b) and 3(c)], where lattice contrast is clearly visible. The cavities are generally small, a few nanometers in diameter. Some of the larger cavities appear to be faceted. Cavities imaged with CB-STEM in lattice resolution have not yet been reported in the literature. Fig. 3(a) shows that He cavities are distributed mainly over the depth region from 100 to 400 nm and nearly disappear at ~450 nm, consistent qualitatively with the SRIM prediction [Fig. 1(a)]. In contrast to the conventional Fresnel fringe contrast from a defocused beam, the CB-STEM technique reveals more details of the cavity shape. Due to the reduced probability of projection effects in the limited depth of focus, the technique enables a greater accuracy in counting the cavities and determining their number density.

Fig. 4(a) shows a similar depth profile of the He cavities in the W phase of the irradiated 87R DPT W. It is apparent that He cavities in W are smaller and have a greater number density than in NiFeW. The cavities are distributed up to the depth of ~350 nm, which is again consistent qualitatively with the SRIM prediction [Fig. 1(b)]. Figs. 4(b) and 4(c) show high-resolution images at selected depths. While lattice contrast is not as obvious near the peak damage region around the depth of 180 nm, pockets of regular lattice can be observed in W close to the ion projected range, where both the damage level and cavity number density are low.

Formation of He cavities in this study includes processes of incubation, nucleation and growth, followed by coarsening during further irradiation to a higher dose. In the process of cavity coarsening, there are two different mechanisms [16]: (1) Ostwald ripening (OR) [43,44] and (2) cavity migration and coalescence (MC) [45,46]. Under the condition of He production and displacement damage during He⁺ ion irradiation at 973 K, the nucleation of He cavities in NiFeW or W occurs by concurrent diffusion and clustering of He atoms and vacancies. He⁺ ions were implanted into W at an intermediate temperature of 973 K, which is between the homologous temperatures $0.2T_m$ and $0.5T_m$ (melting point of W $T_m(W) = 3,695$ K), to a relatively high concentration (7.3 He/cm² in W at the peak maximum) and a low dose (1.1 dpa in W at the peak maximum). Under the irradiation conditions, He atoms are effectively resolved from small bubbles by displacement cascades, resulting in the nucleation of secondary generations of He cavities [47]. At relatively high ratios of He production to displacement rates in NiFeW (6.0 at.% He and 2.6 dpa in NiFeW at their maxima) and at $T > 0.5T_m$ (melting point of NiFeW $T_m(NiFeW)$ [9] approximately equal to that of Ni $T_m(Ni) = 1,728$ K), the nucleation process is governed by the strong dependence of the nucleation rate and the increasing absorption rate [16]. The number density initially increases strongly with increasing He concentration, and then virtually saturates with the average size continuously increasing as more He atoms are implanted into the NiFeW. Therefore, the observed He cavities with a relatively larger size and a lower number density in NiFeW are a result of the dominant process of thermal dissociation of He atoms from small cavities at 973 K in NiFeW.

4.2. He cavity diameter, volume and number density

Detailed analysis of the He cavities in Figs. 3(a) and 4(a) for the diameter and volume distributions as a function of depth has been performed using an in-house developed image processing algorithm. The cavity areas are identified based on the contrast in the contrast-optimized images. The average cavity diameter D_0 and volume V_0 in NiFeW and W are calculated at an increment step of 50 nm in depth. The results for the cavity diameter and volume in NiFeW and W as a function of depth are shown at the same binning size of 0.2 nm in Figs. 5 and 6, respectively. The cavity diameters are in the range from 1.5 to 9.5 nm in NiFeW and from 0.9 to 3.1 nm in W across the entire irradiation region, corresponding to spherical cavity volumes from 1.8 to 448.9 nm³ in NiFeW and from 0.38 to 15.6 nm³ in W. The arithmetic averages of the cavity diameters and volumes are 4.05 nm and 49.0 nm³ in NiFeW and 1.50 nm and 2.1 nm³ in W, in agreement with our previous reports [18,22]. The average diameter and volume of the cavities in NiFeW is ~2.7 and ~23.3 times those in W, respectively.

The average cavity diameters and volumes within each increment of 50 nm in depth are plotted as a function of depth in Fig. 7. In both NiFeW and W, the average diameters are larger around the He concentration peaks. Smaller cavity diameters appear near the surface and the He ion projected range.

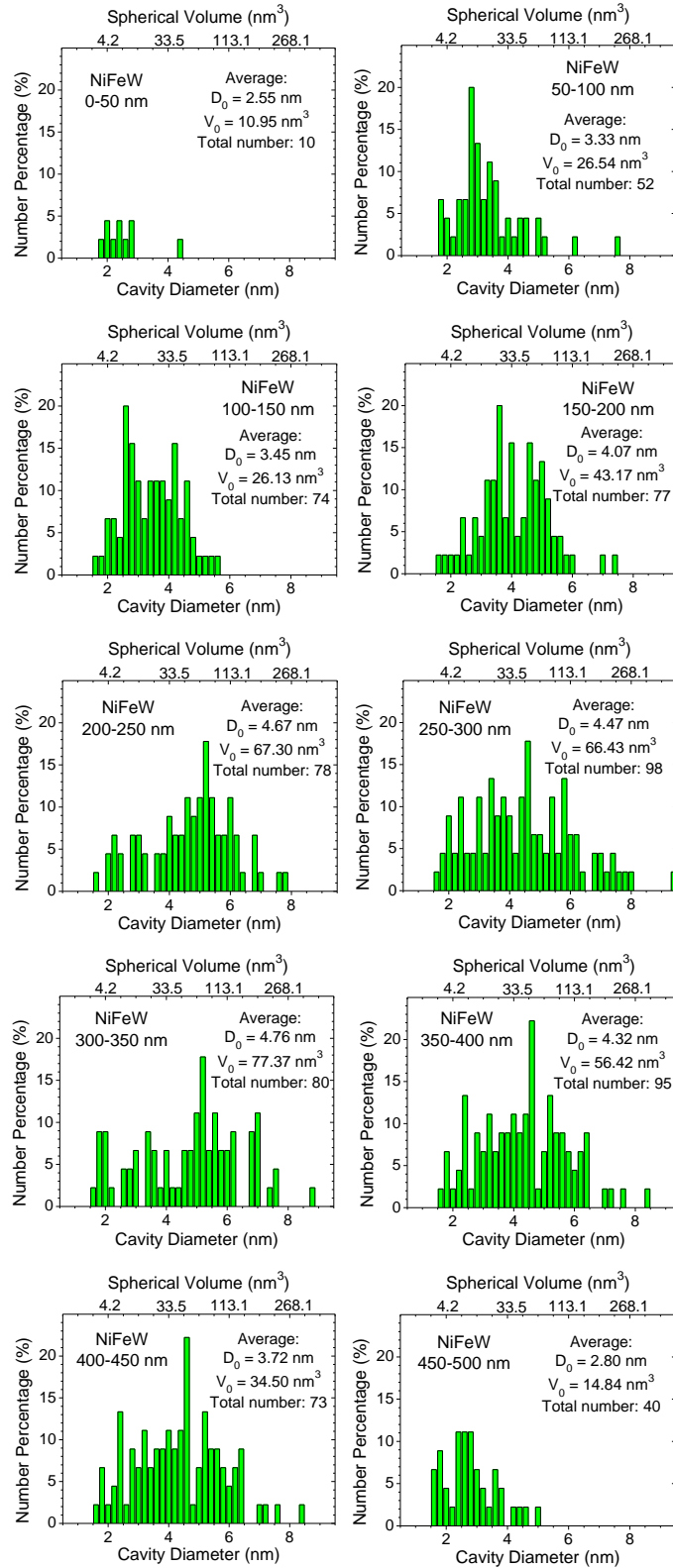


Fig. 5. Histograms for the He cavity diameter and volume distributions in different depth regions of NiFeW within 87R DPT W irradiated with 90 keV He⁺ ions to 1.0×10^{17} He⁺/cm² at 973 K.

The relative number densities of the He cavities as a function of depth in NiFeW and W are determined based on the data in Figs. 5 and 6, respectively. The depth of focus in different areas under a fixed CB-STEM condition remains constant for each of the materials, NiFeW or W. Instead of calculating the absolute value of the depth of focus, which is non-trivial, additional STEM-EELS mapping was performed in extremely thin regions revealing all the cavities throughout the entire foil thickness. The imaging areas in NiFeW and W have the average depths (designated as the geometrical center of the image) of 318 nm and 250 nm with the local foil thickness values of ~ 23 nm and ~ 10 nm, respectively, determined by EELS thickness mapping [48]. The total number of He cavities in the analysis region is 77 over an area of $5.93 \times 10^3 \text{ nm}^2$ in NiFeW and 341 over $3.36 \times 10^3 \text{ nm}^2$ in W, corresponding to the number densities of $5.6 \times 10^{17} \text{ cm}^{-3}$ in NiFeW and $1.0 \times 10^{19} \text{ cm}^{-3}$ in W, respectively. As the number density is same at the same depth in ion-irradiated samples, these values are used to calibrate the relative number density profiles. The quantitative results are shown in Fig. 8. Clearly, the number densities in both NiFeW and W are fairly flat over a large depth region. Compared to the cavity number densities in NiFeW and W within an 87R DPT W irradiated to a lower ion fluence of $6.5 \times 10^{15} \text{ He}^+/\text{cm}^2$ at 973 K [18], which were analyzed with conventional TEM under a defocus condition, this study shows larger values in both materials. Part of the reasons might be that some of the small He cavities could be

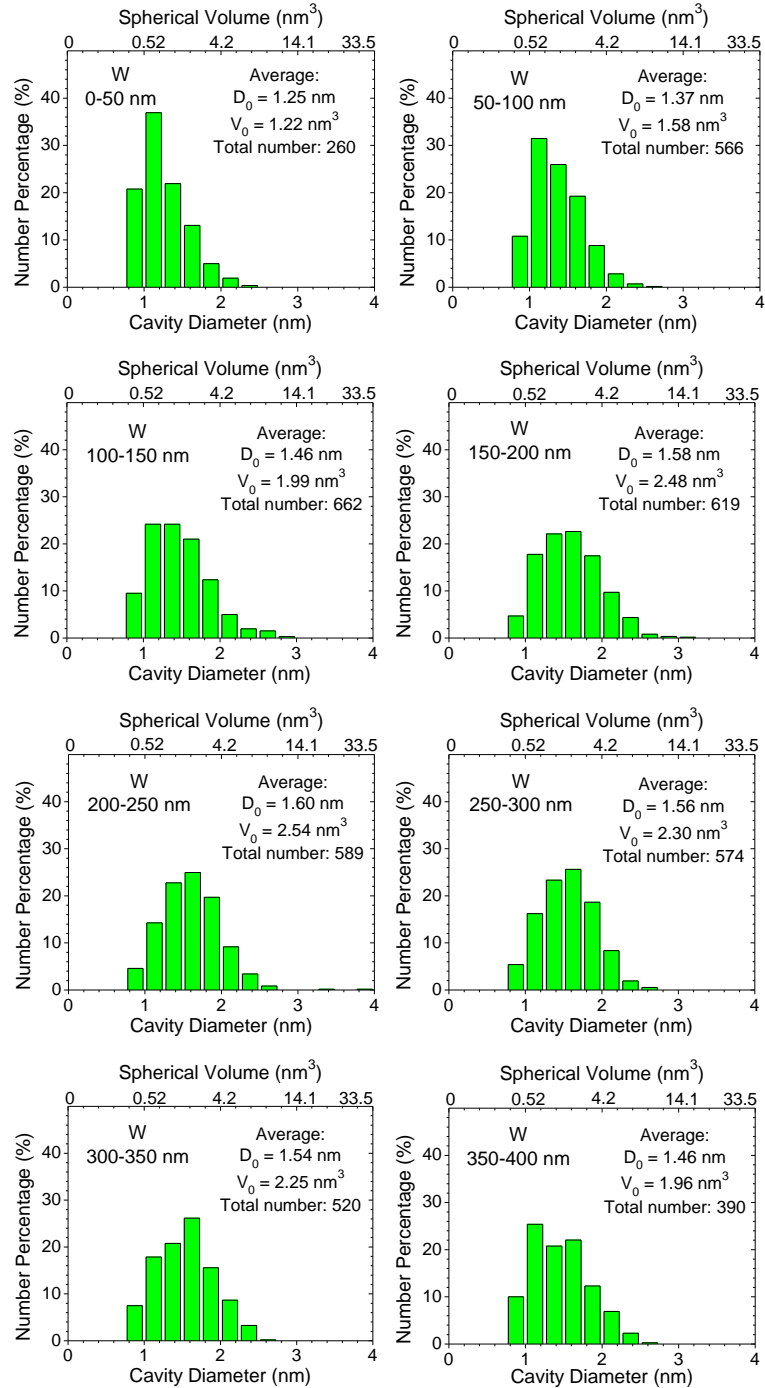


Fig. 6. Histograms for the He cavity diameter and volume distributions in different depth regions of W within 87R DPT W irradiated with 90 keV He^+ ions to $1.0 \times 10^{17} \text{ He}^+/\text{cm}^2$ at 973 K.

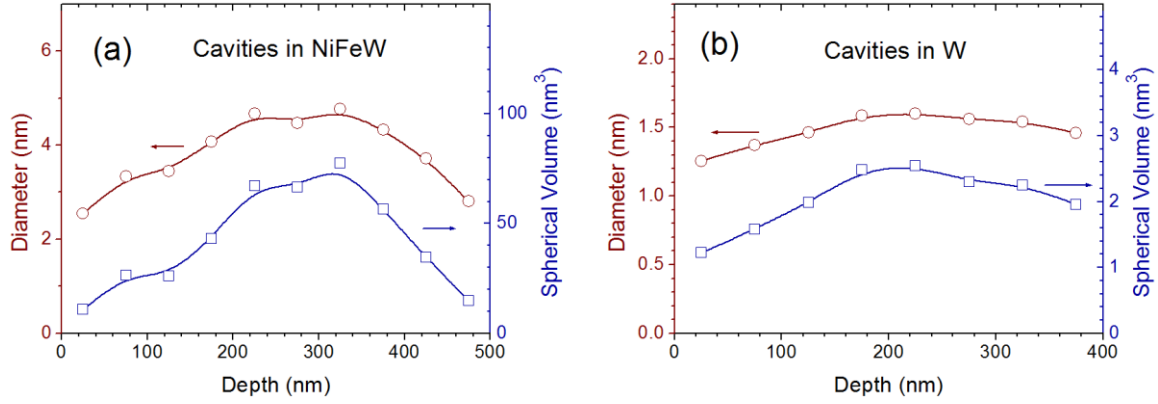


Fig. 7. Depth profiles of the cavity diameter and volume in (a) NiFeW and (b) W within 87R DPT W irradiated with 90 keV He⁺ ions to 1.0×10^{17} He⁺/cm² at 973 K.

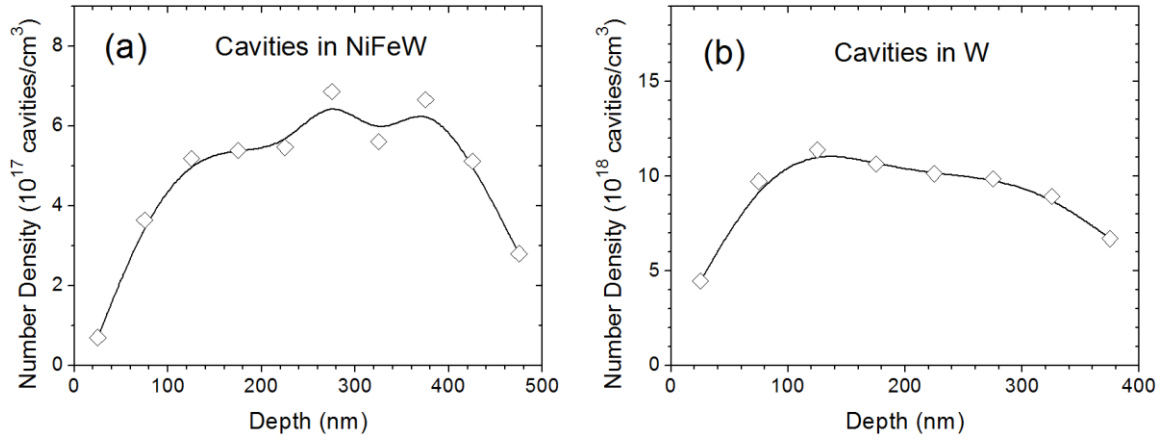


Fig. 8. Depth profiles of the cavity number density in (a) NiFeW and (b) W within 87R DPT W irradiated with 90 keV He⁺ ions to 1.0×10^{17} He⁺/cm² at 973 K.

effectively covered up due to image projection through a larger foil thickness and a potential influence of the pre-existing damage from Ni⁺ ion irradiation in our previous study [18].

It is known that the temperature dependency of cavity densities in metals is similar during irradiation and during post-irradiation thermal annealing [16]. Cavity formation is controlled by He atom and cavity migration and interaction at relatively low temperatures and their dissociation at higher temperatures, depending on specific materials. At an intermediate temperature where He atoms and mono-vacancies are mobile, both the He cavity density and size initially increase with increasing He concentration. With further increase in the vacancy and He concentrations, cavity size continues to increase but cavity number density tends to approach to a saturation value at the temperature partly because migration and coalescence of the cavities becomes more probable. In fact, cavity nucleation occurs in an early stage and then virtually ceases at a certain cavity number density [16]. As a result, cavity number density does not depend on the He concentration as significantly as the average cavity size. This is why the number density profiles in both NiFeW and W show a plateau over a large depth region in Fig. 8. It also explains the behavior of the diameter distribution Fig. 7, where the He cavity diameter is larger at higher He

concentration. In this study, both He atoms and mono-vacancies in NiFeW and W [49,50] are mobile at 973 K, which controls the nucleation and growth processes of the He cavities. In addition to temperature, different doses may also contribute to the difference in the cavity size and number density in W and NiFeW.

4.3. He density and pressure in cavities

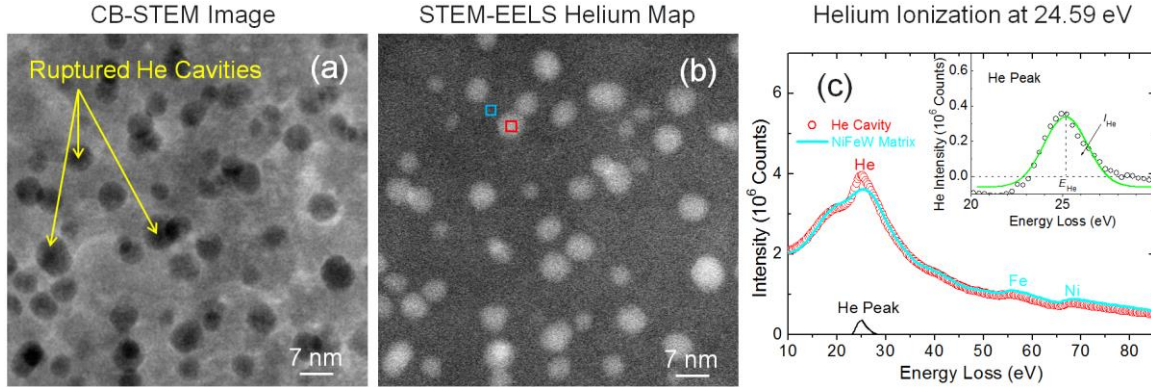


Fig. 9. (a) CB-STEM image, (b) STEM-EELS He map, and (c) EELS spectra from a He cavity and the NiFeW matrix in 87R DPT W irradiated with 90 keV He⁺ ions to 1.0×10^{17} He⁺/cm² at 973 K. The He core-loss peak is the cavity spectrum subtracted by the normalized matrix spectrum. The inset in (c) is a Gaussian fit to the He data with the peak position $E_{He}=25.16$ eV. Integrated intensity $I_{He}=2.89 \times 10^6$ for the He peak and $I_Z=2.00 \times 10^9$ for the zero-loss peak.

Figs. 9(a) and 9(b) show a CB-STEM image and a STEM-EELS He map acquired in the same area, respectively. Most of the He cavities are observed in both figures. However, a few of them that appear in the CB-STEM image are not visible in the STEM-EELS He map, as indicated by arrows in Fig. 9(a). Similar observations were also reported [23,25]. The absence of these cavities in the STEM-EELS map is a result of the cavity rupturing at the specimen surface during FIB preparation of the TEM sample, followed by a complete He release from the cavity. As Fig. 9(b) only shows He-rich regions, these cavities are absent from the image. Fig. 9(c) shows two EELS spectra from the center of a He-filled cavity with a diameter of 5.61 nm and a neighboring area outside the cavity in NiFeW, as indicated in Fig 9(b). He K-line loss peak on top of the plasmon peak and Fe M₂₃ (57 eV) and Ni M₂₃ (68 eV) core-loss peaks are clearly exhibited from the cavity area. There is no energy shift in the zero-loss peaks from the cavity and NiFeW matrix. Intensity normalization of the spectrum from the matrix to the spectrum from the cavity was performed on both sides of the He peak in the energy-loss regions from 10 to 20 eV and from 30 to 40 eV. Subtraction of the former from the latter gives the He core-loss spectrum, as shown in Fig. 9(c). It should be noted that a perfect match of the two EELS spectra in the selected energy regions through the yield normalization procedure may not be achievable because the path length of an electron through a foil with a He cavity depends on the specific location on the cavity. The variation in the foil thickness within the probing area of a cavity can affect the shape of the plasmon peak in the EELS spectrum. While a reduced probing area could decrease the extent of the variation, an increase in the dwelling time of the 300 keV electron beam would be required to minimize the statistical error. This would in turn decrease the He density by ejecting more He atoms in the cavity due to ballistic collision

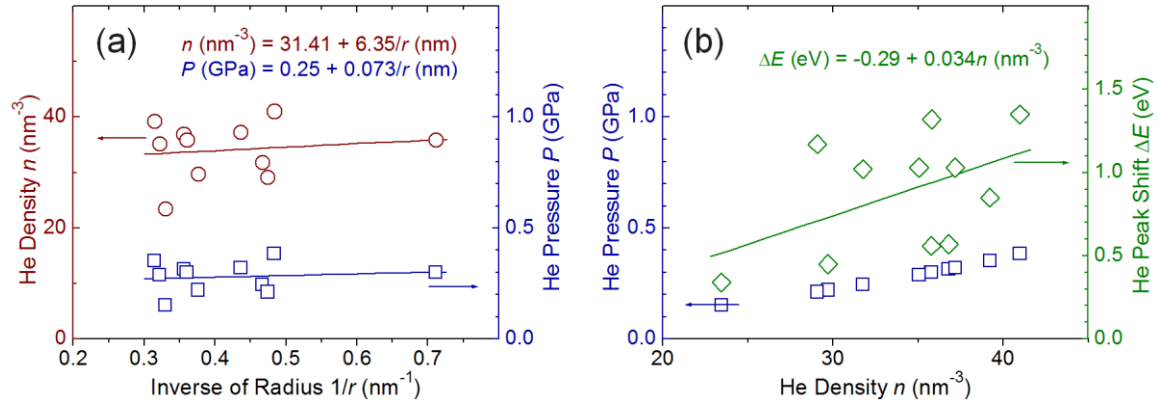


Fig. 10. (a) He density n and pressure P in cavities at 300 K as a function of the reverse of the cavity radius $1/r$ in NiFeW within 87R DPT W irradiated with 90 keV He⁺ ions to 1.0×10^{17} He⁺/cm² at 973 K. (b) He pressure P and He peak shift ΔE as a function of He density n at 300 K.

Table 1

Properties of helium cavities in He⁺ ion irradiated NiFeW determined by STEM-EELS.

Diameter d (nm)	ΔE (eV)	I_{He} ($\times 10^6$)	I_Z ($\times 10^9$)	He density n (at./nm ³)	He density He/V	He pressure P (GPa, 300 K)	Equi. pressure P_e (GPa, 300 K)
2.81	+1.32	1.33418	1.89436	35.81	0.42	0.30	2.70
4.13	+1.35	2.30481	1.94487	40.99	0.48	0.38	1.84
4.21	+1.17	1.65177	1.92671	29.09	0.34	0.21	1.81
4.28	+1.02	1.79317	1.88393	31.77	0.37	0.24	1.78
4.58	+1.03	2.30545	1.93333	37.20	0.43	0.32	1.66
5.31	+0.45	2.21954	2.00869	29.73	0.35	0.22	1.43
5.54	+0.56	2.93886	2.11753	35.79	0.43	0.30	1.37
5.61	+0.57	2.88584	1.99614	36.81	0.42	0.31	1.35
6.05	+0.34	1.97612	1.98968	23.45	0.27	0.15	1.26
6.20	+1.03	2.99036	1.96498	35.07	0.41	0.29	1.23
6.35	+0.85	3.35195	1.92217	39.23	0.46	0.35	1.20

The He energy-loss shift ΔE is relative to the He K-shell ionization energy of 24.59 eV.

I_{He} and I_Z are the integrated intensities of the He core-loss and zero-loss peaks, respectively.

The He/V density in a cavity is calculated based on the mono-vacancy density of 86.09 V/nm³.

The equilibrium pressure is $P_e = 2\gamma/r$ with r being the cavity radius and γ the surface energy taken as 1.9 J/m².

[23]. However, a normalization procedure is needed to make the average foil thickness in the two selected areas approximately equal.

The He core-loss spectrum is fitted with a Gaussian function. The peak maximum is located at 25.16 eV, representing a blue shift of 0.57 eV from the ionization energy (24.59 eV) of a free He atom, as shown in the inset of Fig. 9(c) and listed in Table 1. An energy-loss shift of a He peak from 1s \rightarrow 2p has been observed under 100 keV [25,26] or 200 keV [23,27,28] electron irradiation in a TEM microscope. It was attributed to the effects of He densities in a bubble [28]. While the density effect was evidenced [23], the peak had blue shifts only from 21.2 eV to 22.3 eV, but rarely to a value above 24 eV. In general, a faster-moving electron beam will more likely ionize a He atom. As He cavities were probed with high-energy (300 keV) electron STEM-EELS in this study, the He core-loss peak is likely dominated by He K-shell ionization rather than He 1s \rightarrow 2p excitation. Interestingly, a previous report [28] shows a double-peak structure in the EELS spectrum from 200 keV electron irradiation, which was attributed to 1s \rightarrow 2p

and $1s \rightarrow 3p$ transitions of He atoms in a bubble. The energy-loss shift could originate from both the He density and interface effects, as discussed below.

The integrated intensity of the He peak (I_{He}) is estimated by summing up the positive intensities in the He core-loss peak from 20 to 30 eV. Negative intensities in the counts resulting from the imperfect normalization, as seen in the inset of Fig. 9(c), are excluded from the area estimation. This is expected to create an error of up to ~10% in this study. The integrated intensity of the zero-loss peak (I_z) in the spectrum from the cavity is obtained from -10 to 10 eV. The He density in the cavity is then calculated from Equation (1) using the cross-section of He K-shell ionization. Similar to those in [51], the He K-shell ionization cross section [52] is approximated as $\sigma = 7.0 \times 10^{-24} \text{ m}^2$ under the imaging conditions of this study. The pressure in the cavity is subsequently obtained from Equations (2) and (3). Calculations indicate that the He density and pressure inside a 5.61 nm diameter He cavity in NiFeW is 36.81 at./nm³ and 0.31 GPa at 300 K, respectively, as listed in Table 1. It is noticed that this calculated He density is higher than that of liquid He (0.125 g/cm³ or ~18.8 at./nm³ at the boiling point) as well as solid-state He (0.214 g/cm³ or ~32.2 at./nm³ at 1.15 K and 66 atm, equivalent to ~0.0066 GPa) in some cases. Despite the very high density, helium atoms in the cavities are still expected to be in a fluid state because room temperature is much higher than the critical temperature.

There are two limiting cases that determine the values of the pressure inside a cavity. One is the EOS under a thermodynamic equilibrium, as expressed in Equation (2). The other is the mechanical stability limit of the cavity. For a given radius r of a cavity, the mechanical equilibrium pressure is determined by $P_e = 2\gamma/r$, where γ is the surface free energy of the cavity. Cavities below a radius of r can exist only in the presence of He atoms to balance the surface tension or surface free energy. Above r He atoms are not needed to stabilize the cavity and the pressure P inside the cavity can drop below P_e [24]. At a high He to dpa ratio and a high He concentration, the pressure in a cavity can remain significantly above P_e [16]. An overpressure ($P > P_e$) of He atoms can promote He bubble growth. Previous reports show that $\gamma = 1.8 \text{ J/m}^2$ for Ni(100), 1.9 J/m^2 for Ni(110) [53], and 1.946 J/m^2 for Ni(111) [54]. Taking $\gamma = 1.9 \text{ J/m}^2$ as an approximate value for NiFeW at 300 K, P_e is estimated to be ~1.35 GPa for a cavity with a diameter of 5.61 nm in NiFeW, as listed in Table 1. In addition, NiFeW has a face centered cubic structure (fcc) with a lattice constant of 0.3595 nm [55]. Thus, the mono-vacancy density in a unit cell with 4 atoms or a void of any size in NiFeW corresponds to 86.09 V/nm³. Because the actual He density and pressure in the 5.61 nm sized cavity under the thermal equilibrium condition at 300 K are only 36.81 He/nm³ (or He/V=0.42) and 0.31 GPa, respectively, as listed in Table 1, the He atoms in this cavity are thus under-pressurized.

The He peak shifts, He atomic densities, He/V densities and pressure values from many other cavities in NiFeW in Fig. 9 have also been determined and summarized in Table 1. Data points from areas that show cavity overlapping, vague cavity edges, or abnormal He intensities are excluded from listing in the table. The density values in Table 1 have a similar order of magnitude reported for martensitic steel [25] and zirconium [26]. The overall He/V densities from Table 1 are ~0.4 over the range of relative He concentrations from 0.28 to 0.48 at.% in NiFeW (83.46 at./nm³), comparable to the reported data in Ni [36,56]. The density n and pressure P in the cavities are plotted as a function of the inverse of cavity radius, as shown in Fig. 10(a). Both the n and P data are fitted with a linear function with the inverse of radius. The data fits give $n(\text{He/nm}^3) = 31.41 + 6.35/r(\text{nm})$ and $P(\text{GPa}) = 0.25 + 0.073/r(\text{nm})$. As the slope in the latter data fit is smaller than the free energy of approximately 1.9 J/m^2 for NiFeW, the He atoms in the cavities are under-pressurized. This is consistent with the data in Table 1, where the He pressure P from the EOS at thermodynamic equilibrium [Equations (2) and (3)] is smaller than the corresponding mechanical equilibrium pressure P_e in all the cavities.

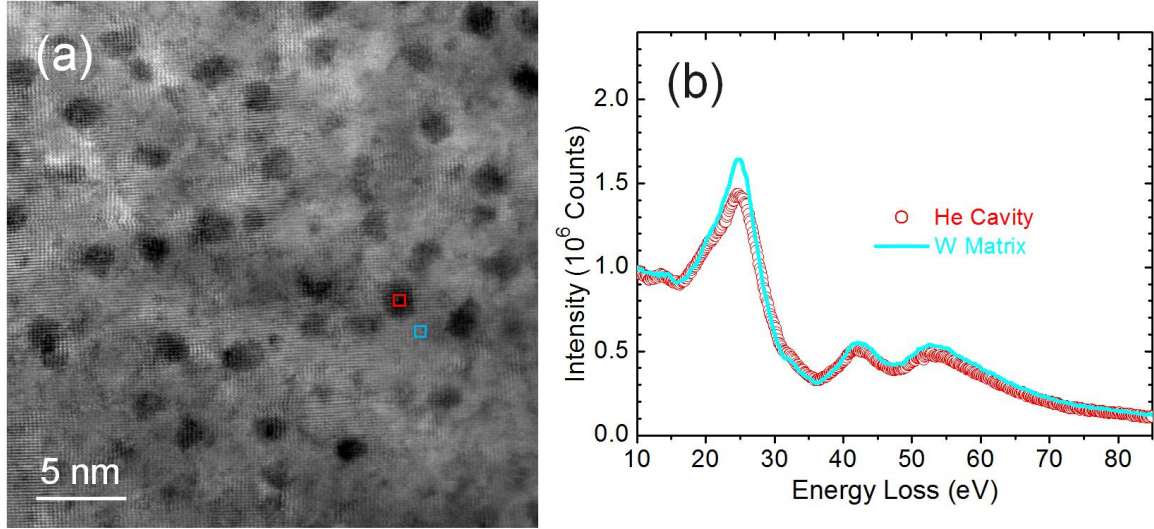


Fig. 11. (a) CB-STEM image and (b) EELS spectra from a He cavity and the W matrix in 87R DPT W irradiated with 90 keV He⁺ ions to 1.0×10^{17} He⁺/cm² at 973 K.

The He energy-loss shifts are also listed in Table 1 with the values ranging from 0.34 to 1.35 eV. This range of blue shifts is consistent with previous reports by others for different materials [25]. Lucas *et al.* [57] have attributed the blue shift of the He *K*-line to the short-range Pauli repulsion between the electrons of neighboring He atoms. This effect is expected to increase linearly with the He density in nanosized bubbles. Jäger *et al.* [58] have also reported a linear relationship in the same year. Consistent behavior was later confirmed in the tritiated Pd₉₀Pt₁₀ matrix [25] and He ion implanted martensitic steel [26]. A linear fit to the He energy-loss shift data in Table 1 gives a result of $\Delta E(\text{eV}) = -0.29 + 0.034n$ (He/nm³), as shown in Fig. 10(b). The slope of 0.034 eV/(He/nm³) for NiFeW is comparable to the reported values for Pd₉₀Pt₁₀ (0.044) [25] and martensitic steel (0.036) [26]. In addition to the high He density effect, the energy-loss shift has also been attributed to the surface excitation due to modifications of the electromagnetic properties of the He atoms close to the metallic interface [25]. Also included in Fig. 10(b) is a plot of He pressure against He density in the cavities. The pressure increases monotonically with increasing density, governed by Equations (2) and (3).

Fig. 11(a) shows a CB-STEM image in W, where some of the He cavities as small as 1 nm can be observed. The broad energy-loss peak at 42 eV in Fig. 11(b) may correspond to the mean core-loss value of W O₂ (47 eV) and O₃ (37 eV) edges [59]. Similarly, the peak at 52 eV may be the mean value of W O₄ and O₅ edges. In contrast to the NiFeW case, a typical EELS spectrum in the He cavity area does not exhibit a resolved He peak, as shown in Fig. 11(b). The peak intensity in the He energy-loss region (20 to 30 eV) from the cavity area is lower than in the normalized EELS spectrum from the neighboring W matrix without a cavity. The darker contrast of the cavities is attributed to the smaller thickness in the local area. Rupture of all the analyzed cavities in Fig. 11(a) during the FIB process can virtually be excluded because similar images from many other areas at different depths also do not reveal any resolvable He signal. Therefore, the He density in the cavity in W, if any, is too low to be detectable under the EELS conditions of this study. However, He cavities are observed for a comparable size in NiFeW, as reported in Table 1. Reasons for the invisibility of the He atoms in W may include that the He *K*-line energy-loss spectrum overlaps with a very strong W plasmon peak, which raises the detection limit. As discussed in section 4.1, the irradiation temperature (973 K) of this study corresponds to a

homologous temperature of only $0.26T_m$ in W. The dominant process at this temperature under the He^+ ion irradiation conditions of this study is the nucleation of small cavities with little thermal dissociation of He atoms from them, which leads to the formation of small cavities and a large number density.

5. Conclusions

This study reports on the behavior and properties of the He-filled cavities formed in an 87R DPT W composite after irradiation with 90 keV He^+ ions to $1.0 \times 10^{17} \text{ He}^+/\text{cm}^2$ at 973 K. He cavities in both NiFeW and W phases are examined at an atomic-scale resolution using CB-STEM. Compared to the conventional TEM under a defocus condition, this methodology offers several advantages, including revealing the delicate microstructures of nanometer-sized cavities, a correction-free measurement of the cavity diameters, and a more accurate analysis of cavity number densities. The results from this study show that the diameters of the cavities in both phases are larger in the depth region around the He concentration peak because cavities grow faster at a higher He concentration. The number density profile is relatively flat in a broad depth region due to cavity size saturation at the applied temperature (973 K). The He cavity diameters in NiFeW range from 2.5 to 4.8 nm with an average value of $\sim 4.05 \text{ nm}$, which is ~ 2.7 times that in W. The number density of the He cavities in NiFeW is $\sim 6 \times 10^{17} \text{ cavities}/\text{cm}^3$, which is an order of magnitude lower than in W ($\sim 1 \times 10^{19} \text{ cavities}/\text{cm}^3$). This behavior is a result of the dominant process of thermal dissociation of He atoms from small cavities at 973 K in NiFeW. Both the He density and pressure in the cavities in NiFeW are quantified using spatially resolved STEM-EELS mapping. They both follow a linear relationship with the inverse of the cavity radius. The He atoms in the cavities in NiFeW are found to be under-pressurized. The He energy-loss shift exhibits a linear relationship with the He density in NiFeW, showing a similar slope to that for martensitic steel. As the He core-loss peak in W cannot be resolved in this study, He density or pressure in the cavities cannot be determined. Further investigation of the cavity behavior in DPT W, including interphase boundaries, is being performed as a function of temperature, He ion flux and dose rate to better understand the mechanisms of nucleation and growth of He cavities in this promising fusion candidate material.

Declaration of Competing Interest

The authors declare that they have no known competing financial interests or personal relationships that could have appeared to influence the work reported in this paper.

Acknowledgements

This research was supported by Office of Fusion Energy Sciences, U.S. Department of Energy (DOE) and performed at the Pacific Northwest National Laboratory under Contract DE-AC05-76RL01830. A portion of the research was performed under a general user proposal of the Environmental Molecular Sciences Laboratory, a DOE Office of Science User Facility located at PNNL. The authors are grateful to Charles Henager for providing 87R DPT W samples for this study.

References

- [1] E. Lassner, W.S. Schubert, Tungsten: properties, chemistry, technology of the element, alloys and chemical compounds, Springer, New York, NY, 1999. P.30.
- [2] R.A. Causey, T.J. Venhaus, The use of tungsten in fusion reactors: a review of the hydrogen retention and migration properties, *Phys. Scr.* T94 (2001) 9.
- [3] S.J. Zinkle, J.T. Busby, Structural materials for fission & fusion energy, *Mater. Today* 12 (2009) 12.
- [4] D.M. Duffy, Fusion power: a challenge for materials science, *Phil. Trans. R. Soc. A* 368 (2010) 3315.
- [5] M. Rieth, S.L. Dudarev, S.M. Gonzalez de Vicente, J. Aktaa, T. Ahlgren, S. Antusch, D.E.J. Armstrong, M. Balden, N. Baluc, M.-F. Barthe, W.W. Basuki, M. Battabyal, C.S. Becquart, D. Blagoeva, H. Boldyryeva, J. Brinkmann, M. Celino, L. Ciupinski, J.B. Correia, A. De Backer, A. Zivelonghi, Recent progress in research on tungsten materials for nuclear fusion applications in Europe, *J. Nucl. Mater.* 432 (2013) 482.
- [6] R.G. Abernethy, Predicting the performance of tungsten in a fusion environment: a literature review, *Mater. Sci. Technol.* 33 (2017) 388.
- [7] H. Ullmaier, F. Carsughi, Radiation damage problems in high power spallation neutron sources, *Nucl. Instrum. Methods Phys. Res. B.* 101 (1995) 406.
- [8] M. Rieth, J.L. Boutard, S.L. Dudarev, T. Ahlgren, S. Antusch, N. Baluc, M.-F. Barther, C.S. Becquart, L. Ciupinski, J.B. Correia, C. Domain, J. Fikar, E. Fortuna, C.-C. Fu, E. Gaganidze, T.L. Galán, C. García-Rosales, B. Gludovatz, H. Greuner, K. Heinola, M.A. Yar, Review on the EFDA programme on tungsten materials technology and science, *J. Nucl. Mater.* 417 (2011) 463.
- [9] C.H. Henager, Jr., W. Setyawan, T.J. Roosendaal, N.R. Overman, B.A. Borlaug, E.L. Stevens, K.B. Wagner, R.J. Kurtz, G.R. Odette, B.N. Nguyen, K. Cunningham, Ductile-phase toughened tungsten for plasma-facing materials in fusion reactors, *Int. J. Powder Metall.* 53 (2017) 53.
- [10] R. Neu, H. Maier, M. Balden, R. Dux, S. Elgeti, H. Gietl, H. Greuner, A. Herrmann, T. Höschen, M. Li, V. Rohde, D. Ruprecht, B. Sieglin, I. Zammuto, ASDEX Upgrade Team, Results on the use of tungsten heavy alloys in the divertor of ASDEX Upgrade, *J. Nucl. Mater.* 511 (2018) 567.
- [11] M.E. Alam, G.R. Odette, On the remarkable fracture toughness of 90 to 97W-NiFe alloys revealing powerful new ductile phase toughening mechanisms, *Acta Mater.* 186 (2020) 324.
- [12] J.V. Haag IV, D.J. Edwards, C.H. Henager Jr., W. Setyawan, J. Wang, M. Murayama, Characterization of ductile phase toughening mechanisms in a hot-rolled tungsten heavy alloy, *Acta Mater.* 204 (2021) 116523.
- [13] J.V. Haag IV, J. Wang, K. Kruska, M.J. Olszta, C.H. Henager Jr., D.J. Edwards, W. Setyawan, M. Murayama, Investigation of interfacial strength in nacre-mimicking tungsten heavy alloys for nuclear fusion applications, *Sci. Rep.* 13 (2023) 575. <https://doi.org/10.1038/s41598-022-26574-4>
- [14] M.R. Gilbert, J.-Ch. Sublet, Neutron-induced transmutation effects in W and W-alloys in a fusion environment, *Nucl. Fusion* 51 (2011) 043005.
- [15] Fusion Evaluated Nuclear Data Library Ver.3.1d (FENDL-3.1d) at <https://www-nds.iaea.org/fendl/>.
- [16] H. Trinkaus, B.N. Singh, Helium accumulation in metals during irradiation – where do we stand? *J. Nucl. Mater.* 323 (2003) 229.
- [17] H. Ullmaier, The influence of helium on the bulk properties of fusion reactor structural materials, *Nucl. Fusion* 24 (1984) 1039.
- [18] W. Jiang, D. Zhang, D. Li, J. Heo, Z. Wang, L.M. Zhang, N. Overman, T. Varga, Z. Hu, X. Wang, L. Shao, W. Setyawan, Behavior of helium cavities in ion-irradiated W-Ni-Fe ductile-phase toughened tungsten, *J. Nucl. Mater.* 561 (2022) 153565.
- [19] T. Wang, H. Kim, X. Wang, A.M. Pacheco, F.A. Garner, L. Shao, Helium retention, bubble superlattice formation and surface blistering in helium-irradiated tungsten, *J. Nucl. Mater.* 545 (2021) 152722.
- [20] J. Zhang, W. Jiang, Z. Zhu, L. Shao, L. Price, J. Zhao, T. Wang, Thermal annealing behavior of hydrogen and surface topography of H₂⁺ ion implanted tungsten, *J. Nucl. Mater. Tech.* 55 (2018) 703.

- [21] J. Zhang, J. Zhao, W. Jiang, X. Guan, H. Peng, Z. Zhu, T. Wang, Formation of bubbles and blisters in hydrogen ion implanted polycrystalline tungsten, *Rad. Eff. Def. Solids* 173 (2018) 1027.
- [22] W. Jiang, Y. Zhu, L. Zhang, D.J. Edwards, N.R. Overman, G. Nandipati, W. Setyawan, C.H. Henager Jr., R.J. Kurtz, Dose rate effects on the damage accumulation and void growth in self-ion irradiated tungsten, *J. Nucl. Mater.* 550 (2021) 152905.
- [23] M.-L. David, K. Alix, F. Pailloux, V. Mauchamp, M. Couillard, G.A. Botton, L. Pizzagalli, *In situ* controlled modification of the helium density in single helium-filled nanobubbles, *J. Appl. Phys.* 115 (2014) 123508.
- [24] C.A. Walsh, J. Yuan, L.M. Brown, A procedure for measuring the helium density and pressure in nanometre-sized bubbles in irradiated materials using electron-energy-loss spectroscopy, *Philos. Mag. A* 80 (2000) 1507.
- [25] D. Taverna, M. Kociak, O. Stéphan, A. Fabre, E. Finot, B. Décamps, C. Collie, Probing physical properties of confined fluids within individual nanobubbles, *Phys. Rev. Lett.* 100 (2008) 035301.
- [26] S. Fréhard, M. Walls, M. Kociak, J.P. Chevalier, J. Henry, D. Gorse, Study by EELS of helium bubbles in a martensitic steel, *J. Nucl. Mater.* 393 (2009) 102.
- [27] M.S. Blackmur, S. Dumbill, I. MacLaren, D. Hernandez-Maldonado, P.D. Stymana, M. Gass, R.J. Nicholls, J.M. Hyde, Q.M. Ramasse, K.J. Annand, J.S. Smith, N. Gothamf, The association of hydrogen with nanometre bubbles of helium implanted into zirconium, *Scripta Mater.* 152 (2018) 102.
- [28] M. Klimenkov, P. Vladimirov, J. Hoffmann, N. Zimmer, A. Möslang, V. Kuksenkov, First simultaneous detection of helium and tritium inside bubbles in beryllium, *Micron* 127 (2019) 102754.
- [29] E. Torres, C. Judge, H. Rajakumar, A. Korinek, J. Pencer, G. Bickel, Atomistic simulations and experimental measurements of helium nano-bubbles in nickel, *J. Nucl. Mater.* 495 (2017) 475.
- [30] L. Sandoval, D. Perez, B.P. Uberuaga, A.F. Voter, Competing kinetics and He bubble morphology in W, *Phys. Rev. Lett.* 114 (2015) 105502.
- [31] J. Cui, M. Li, J. Wang, Q. Hou, Molecular dynamics study of helium bubble pressure in tungsten, *Nucl. Instr. Meth. Phys. Res. B* 352 (2015) 104.
- [32] S. Blondel, D.E. Bernholdt, K.D. Hammond, B.D. Wirth, Continuum-scale modeling of helium bubble bursting under plasma-exposed tungsten surfaces, *Nucl. Fusion* 58 (2018) 126034.
- [33] K.D. Hammond, I.V. Naeger, W. Widanagamaachchi, L.T. Lo, D. Maroudas, B.D. Wirth, Helium flux effects on bubble growth and surface morphology in plasma-facing tungsten from large-scale molecular dynamics simulations, *Nucl. Fusion* 60 (2020) 129401.
- [34] K.D. Hammond, D. Maroudas, B.D. Wirth, Theoretical model of helium bubble growth and density in plasma-facing metals, *Sci. Rep.* 10 (2020) 2192.
- [35] G. Nandipati, K.D. Hammond, D. Maroudas, K.J. Roche, R.J. Kurtz, B.D. Wirth, W. Setyawan, Effect of helium flux on near-surface helium accumulation in plasma-exposed tungsten, *J. Phys.: Condens. Mater.* 34 (2022) 035701.
- [36] S.E. Donnelly, The density and pressure of helium in bubbles in implanted metals: a critical review, *Rad. Eff.* 90 (1985) 1.
- [37] J.F. Ziegler, J.P. Biersack, U. Littmark, *The stopping and Range of Ions in Solids* (Pergamon Press, New York, 1985); available at: <http://www.SRIM.org/>.
- [38] ASTM, ASTM Standard E521-96 (2009), *Standard Practice for Neutron Radiation Damage Simulation by Charged-Particle Irradiation*, ASTM International, West Conshohocken, PA (2009)
- [39] R.E. Stoller, M.B. Toloczko, G.S. Was, A.G. Certain, S. Dwaraknath, F.A. Garner, On the use of SRIM for computing radiation damage exposure, *Nucl. Instrum. Meth. Phys. Res. B* 310 (2013) 75; Erratum to “On the use of SRIM for computing radiation damage exposure” [*Nucl. Instrum. Methods Phys. Res. B* 310 (2013) 75–80], *Nucl. Instrum. Meth. Phys. Res. B* 459 (2019) 196.
- [40] L. Van Brutzel, A. Chartier, A new equation of state for helium nanobubbles embedded in UO₂ matrix calculated via molecular dynamics simulations, *J. Nucl. Mater.* 518 (2019) 431.

- [41] E. Thiele, Equation of State for Hard Spheres, Equation of state for hard spheres, J. Chem. Phys. 39 (1963) 474; M.S. Wertheim, Exact solution of the Percus-Yevick integral equation for hard spheres, Phys. Rev. Letters 10 (1963) E501; M.S. Wertheim, Analytic solution of the Percus-Yevick equation, J. Math. Phys. 5 (1964) 643.
- [42] I.R. Brearley, D.A. MacInnes, An improved equation of state for inert gases at high pressures, J. Nucl. Mater. 95 (1980) 239.
- [43] G.W. Greenwood, A. Boltax, The role of fission gas re-solution during post-irradiation heat treatment, J. Nucl. Mater. 5 (1962) 234.
- [44] A.J. Markworth, On the coarsening of gas-filled pores in solids, Met. Trans. 4 (1973) 2651.
- [45] E.E. Gruber, Calculated size distributions for gas bubble migration and coalescence in solids, J. Appl. Phys. 38 (1967) 243.
- [46] P.J. Goodhew, S.K. Tyler, Helium bubble behaviour in bcc metals below $0.65T_m$, Proc. Roy. Soc. London A 377 (1981) 151.
- [47] P. Dauben, R.P. Wahi, H. Wollenberger, Bubble nucleation and growth in an Fe-12 at% Cr ferritic alloy under He^+ implantation and Fe^+ irradiation, J. Nucl. Mater. 141–143 (1986) 723.
- [48] T. Malis, S.C. Cheng, R.F. Egerton, EELS log-ratio technique for specimen-thickness measurement in the TEM, J. Electron Microsc. Tech. 8 (1988) 193.
- [49] O.V. Ogorodnikova, L. Yu Dubov, S.V. Stepanov, D. Terentyev, Yu.V. Funtikov, Yu.V. Shtotsky, V.S. Stolbunov, V. Efimov, K. Gutorov, Annealing of radiation-induced defects in tungsten: positron annihilation spectroscopy study, J. Nucl. Mater. 517 (2019) 148.
- [50] Z. Hu, P. Desgardin, C. Genevois, J. Joseph, B. Décamps, R. Schäublin, M-F. Barthe, Effects of purity on the vacancy defects induced in self-irradiated tungsten: a combination of APS and TEM, J. Nucl. Mater. 556 (2021) 153175.
- [51] R. Schierholz, B. Lacroix, V. Godinho, J. Caballero-Hernández, M. Duchamp, A. Fernández, STEM–EELS analysis reveals stable high-density He in nanopores of amorphous silicon coatings deposited by magnetron sputtering, Nanotechnology 26 (2015) 075703.
- [52] R.F. Egerton, *Electron Energy-Loss Spectroscopy in the Electron Microscope*, Third edition, Appendix B, Springer, NY (2011).
- [53] P.S. Maiya, J.M. Blakely, Surface self-diffusion and surface energy of nickel, J. Appl. Phys. 38 (1967) 698.
- [54] W.-B. Zhang, C. Chen, S.-Y. Zhang, Equilibrium crystal shape of Ni from first principles, J. Phys. Chem. C 117 (2013) 21274.
- [55] B.C. Muddle, D.V. Edmonds, Precipitation in a liquid phase sintered W–Ni–Fe alloy, *Acta Metall.* 33 (1985) 2119.
- [56] A. Garber, P. Ehrhart, Investigation of the behaviour of helium and radiation defects after room temperature he-implantation of nickel and copper, Rad. Eff. 78 (1983) 213.
- [57] A. Lucas, J. Vigneron, S. Donnelly, J. Rife, Theoretical interpretation of the vacuum ultraviolet reflectance of liquid helium and of the absorption spectra of helium microbubbles in aluminum, Phys. Rev. B 28 (1983) 2485.
- [58] W. Jäger, R. Manzke, H. Trinkaus, R. Zeller, J. Fink, G. Crecelius, The density and pressure of helium in bubbles in metals, Radiat. Eff. 78 (1983) 315.
- [59] R.F. Egerton, *Electron Energy-Loss Spectroscopy in the Electron Microscope*, Third edition, Appendix D, Springer, NY (2011).